Synergistic enhancement of photocatalytic molecular oxygen activation by nitrogen defect and interfacial photoelectron transfer over Z-scheme α-Fe$_2$O$_3$/g-C$_3$N$_4$ heterojunction

Lina Su [a,b,1], Pengfei Wang [c,1], Mingmei Li [a], Zhiyong Zhao [a], Yi Li [d,*], Sihui Zhan [a]

[a] *MOE Key Laboratory of Pollution Processes and Environmental Criteria/Tianjin Key Laboratory of Environmental Remediation and Pollution Control, College of Environmental Science and Engineering, Nankai University, Tianjin 300350, PR China*
[b] *State Key Laboratory of Chemistry and Utilization of Carbon Based Energy Resources, College of Chemistry, Xinjiang University, Urumqi, Xinjiang 830017, PR China*
[c] *Tianjin Key Laboratory of Clean Energy and Pollutant Control, School of Energy and Environmental Engineering, Hebei University of Technology, Tianjin 300401, PR China*
[d] *Tianjin Key Laboratory of Molecular Optoelectronic Sciences, Department of Chemistry, School of Science, Tianjin University & Collaborative Innovation Center of Chemical Science and Engineering, Tianjin 300072, PR China*

ARTICLE INFO

ABSTRACT

Photoinduced molecular oxygen activation offers a promising strategy for oxidative degradation of organic pollutants, but the critical step of oriented electron delivery from the active sites into the stable O$_2$ molecules presents a considerable challenge. Herein, we report the construction of a direct Z-scheme heterojunction with abundant nitrogen defects (α-Fe$_2$O$_3$/g-C$_3$N$_4$) for powering molecular oxygen activation by steering a specific migration route. This specific interfacial photoelectron transfer pathway showcases the establishment of an effective sequential photoelectron transfer channels between α-Fe$_2$O$_3$ and g-C$_3$N$_4$. The nitrogen defects on the g-C$_3$N$_4$ surface can not only serve as the oxygen adsorption sites, but also can act as the terminal electron sink to donate photoexcited high-energy electrons to the adsorbed O$_2$. Therefore, the optimized α-Fe$_2$O$_3$/g-C$_3$N$_4$ exhibits greatly enhanced catalytic performance for molecular oxygen activation, and the degradation rate constant of tetracycline is 4.7 and 12 times higher than g-C$_3$N$_4$ and α-Fe$_2$O$_3$, respectively.

1. Introduction

Globally, antibiotics in water impose an enormous burden on ecosystems and human public health security [1]. For decades, advanced oxidation processes (AOPs) have been shown to be promising strategies for intensive environmental remediation [2]. In particular, with the help of semiconductors, the utilization of photoexcited high-energy electrons to drive molecular oxygen to produce renewable reactive oxygen species (ROS) is considered to be an effective strategy for antibiotics removal [3,4]. However, the conversion efficiency of O$_2$ is thwarted to a large extent by the high carrier recombination efficiency and poor oxygen adsorption capacity in most traditional catalysts [5,6]. Facilitating the delivery of photoexcited electrons from the active sites on catalyst surface to the stably adsorbed O$_2$ molecules is the critical step to obtain a highly active catalyst [7]. Hence, it is of great significance to explore optimization strategy of electron injection into O$_2$ molecular for boosting molecular oxygen activation performance.

As a metal-free material, carbon nitride (g-C$_3$N$_4$) is provoking tremendous interest in the field of heterogeneous photocatalysis owing to its desirable thermal and chemical stability, favorable band structure and facile synthesis process [8–10]. However, pristine g-C$_3$N$_4$ suffers from low photogenerated carrier separation efficiency and reactivity to reactants [11,12]. For decades, various strategies have been explored to circumvent the above challenges, such as morphology control [13], heteroatoms doping [14], creation of heterojunctions [15] and defect engineering [16]. Recently, the advantages of nitrogen defects in photocatalytic redox has aroused the interest of researchers, it is found that the surface nitrogen defects could serve as electron traps and O$_2$ adsorption sites in g-C$_3$N$_4$ heptazine framework, enhancing the interaction between molecular oxygen and semiconductor [17,18]. However, the mismatch between photogenerated carrier lifetimes and oxygen redox kinetics in this single-component semiconductors materials still

---

* Corresponding author.
  E-mail address: liyi@tju.edu.cn (Y. Li).
1 These authors contributed equally to this work.

leads to poor electron mobility and substantial charge recombination during the photocatalytic molecular O_2 activation processes [19]. These drawbacks severely compromise its overall attractiveness despite the superiorities conferred by its photocatalytic oxygen activation performance.

In this case, constructing suitable heterojunction is an effective approach to enhance the carrier separation efficiency and steer charge transfer to achieve a specific migration route [20]. In particular, an emerging Z-scheme heterojunction is revealed to preserve maximum oxidation/reduction potential and unique internal electric field (IEF) mechanism of hetero-structure system [21]. Specifically, they usually consist of reduced and oxidized semiconductor with staggered band structure configurations, which can ensure the spatial separation of redox sites and energetic redox capabilities of carriers. Inspired by this, we speculated that the selection of the appropriate semiconductor to construct a defect mediated Z-scheme g-C_3N_4-based heterojunction catalysts can drive efficient molecular oxygen activation process.

Herein, we develop a novel defect-mediated Z-scheme α-Fe_2O_3/g-C_3N_4 heterojunction as an efficient catalyst to boost photocatalytic molecular O_2 activation. From the in-situ irradiated X-ray photoelectron spectroscopy (IS-XPS), electron paramagnetic resonance (EPR) and first-principles theoretical calculations (DFT), we prove that the built-in electric field at the heterointerface between α-Fe_2O_3 and g-C_3N_4 induces the Z-scheme interfacial charge migration pathway. The abundant nitrogen vacancies on the g-C_3N_4 surface can not only serve as the oxygen adsorption sites, but also can act as the terminal electron sink to donate photoexcited high-energy electrons to the adsorbed O_2. This novel strategy constructs a highly active system of O_2 activation over defect-mediated heterojunction, and shows excellent performance in degradation of tetracycline (TC). In addition, possible environmental risks caused by TC and reaction intermediates were assessed in depth.

2. Experimental section

2.1. Materials preparation

2.1.1. Preparation of carbon nitride (g-C_3N_4)
In this work, g-C_3N_4 was synthesized by thermal polymerization. In a typical case, 2 g melamine was placed in a crucible, heated in a muffle furnace at the heating rate of 2 ℃/min for 4 h, then heated to 550 ℃. The resulting yellow solid were ground into a powder for use.

2.1.2. Preparation of α-Fe_2O_3
α-Fe_2O_3 nanosheets were prepared by a simple hydrothermal approach [22]. In details, 0.273 g $FeCl_3 \cdot H_2O$ was mixed in 0.7 mL H_2O and 10 mL CH_3CH_2OH solution under magnetic stirring. After adding 0.8 g CH_3COONa, the admixture was transferred to Teflon lined stainless steel autoclave and heated at 180 ℃ for 12 h. Finally, the precipitate was collected by filtration, and washed with ultra-pure water for three times. The final product was dried overnight at 60 ℃.

2.1.3. Preparation of α-Fe_2O_3/g-C_3N_4 heterojunction composites
α-Fe_2O_3/g-C_3N_4 heterojunction were synthesized by in situ production of carbon nitride. In details, 2 g melamine powder was dissolved in a certain amount of α-Fe_2O_3-aqueous solution and stirred evenly. Then, the obtained mixture was calcined at 550 ℃ for 4 h with a heating rate of 2 ℃/min. Finally, the obtained product was ground and re-calcined at 550 ℃ for 90 min. The defect-mediated α-Fe_2O_3/g-C_3N_4 heterojunction composites with different amounts (0.5 mL, 1 mL, 2 mL, 4 mL, 8 mL, 0.2 mg/mL) of α-Fe_2O_3 was denoted as 0.1α-Fe_2O_3/g-C_3N_4, 0.2α-Fe_2O_3/g-C_3N_4, 0.4α-Fe_2O_3/g-C_3N_4, 0.8α-Fe_2O_3/g-C_3N_4 and 1.6α-Fe_2O_3/g-C_3N_4, respectively. Among them, the 0.8α-Fe_2O_3/g-C_3N_4 was selected as the model catalyst as it had best performance (denoted as α-Fe_2O_3/g-C_3N_4).

2.2. Molecular oxygen activation measurements

In the typical reaction process, the aqueous suspension of the photocatalyst (1 mL, 10 g/L) and 0.4 mL of 3,3′,5,5′-tetramethylbenzidine (TMB, 50 mM aqueous solution) were dispersed in 0.04 L HAc/NaAc buffer solution. A 300 W xenon lamp with a 420 nm cutoff filter was used as the experimental light source. The UV–vis spectrum (the absorbance around 370 nm) was used to monitor the absorbance of reactants at different time intervals to evaluate the oxidation of TMB. In order to determine the types of reactive oxygen species, the same procedure experiments with different type of scavengers were carried out. In addition, the water in nitrogen feeding tests was boiled before feeding N_2 to remove dissolved oxygen, and catalyst and other chemicals should not be added until it was cooled down to room temperature.

2.3. Degradation experiment

Here, we evaluate the photocatalytic performance of the synthesized catalysts by degrading TC under visible light irradiation. Briefly, 50 mg catalyst was added into 100 mL 20 mg/mL TC aqueous solution. Frist, the suspension was magnetically stirred in dark for 30 min to establish the adsorption-desorption equilibrium. Afterwards, the suspension was top-irradiated under 300 W Xe lamp (CEL-HXUV300E, China) equipped with a 420 nm cutoff filter. 4 mL suspension was extracted and centrifuged at regular intervals, and the absorbance was further determined by UV–vis spectrophotometer (the absorbance around 360 nm).

### 2.4. Theoretical calculation

Density function theory (DFT) were conducted by using the Vienna ab initio Simulation Package (VASP) with the projector augment wave (PAW) potentials method [23]. The energy cutoff energy was set to as of 500 eV. The exchange-correlation effect was described by the generalized gradient approximation of the Perdew-Burke-Ernzerhof functional (GGA-PBE) [24]. For all the calculations, the convergence criteria for the energy and force were set to 1×10^{-5} eV and 0.02 eV Å^{-1}, respectively. The Fermi levels (E_f) of α-Fe_2O_3 (001) and g-C_3N_4 (001) surface were calculated based on the equation of $E_{vac} - E_f = \Phi$, in which Φ is the work function and E_{vac} is the energy of vacuum level.

3. Results and discussion

3.1. Microstructure and chemical properties

The synthesis route of α-Fe_2O_3/g-C_3N_4 heterojunction composites is schematically depicted in Fig. S1. Firstly, the α-Fe_2O_3 nanosheet sample was simply synthesized via a hydrothermal method. Afterward, α-Fe_2O_3 dispersion was mixed with melamine and calcined at 550 ℃ for 4 h to obtain the hybrid α-Fe_2O_3/multilayer g-C_3N_4. Subsequently, heterojunction composite was obtained by secondary calcination. The α-Fe_2O_3/g-C_3N_4 with different amounts (0.5 mL, 1 mL, 2 mL, 4 mL, 8 mL, 0.2 mg/mL) of α-Fe_2O_3 was denoted as 0.1α-Fe_2O_3/g-C_3N_4, 0.2α-Fe_2O_3/g-C_3N_4, 0.4α-Fe_2O_3/g-C_3N_4, 0.8α-Fe_2O_3/g-C_3N_4 and 1.6α-Fe_2O_3/g-C_3N_4, respectively.

To verify the successful preparation of the α-Fe_2O_3/g-C_3N_4 heterojunction composites, the morphology and microstructure of representative photocatalysts were observed by Scanning electron microscopy (SEM) and Transmission electron microscopy (TEM). From the TEM images of α-Fe_2O_3 crystals, α-Fe_2O_3 nanosheets present uniform hexagonal shape with a transverse size of about 210 nm and a thickness of about 18 nm (Fig. S2 and S3). As displayed in Fig. 1a, the lattice spacing of ~0.25 nm corresponded to (110) planes of α-Fe_2O_3 [25]. Whereas the pristine g-C_3N_4 shows a layered structure with no obvious lattice fringes (Fig. S4). As shown in Fig. S5, the heterojunction samples show a significant layered structure, and the dispersion of α-Fe_2O_3 on g-C_3N_4 nanosheets is observed at low-magnification TEM image (Fig. S6).
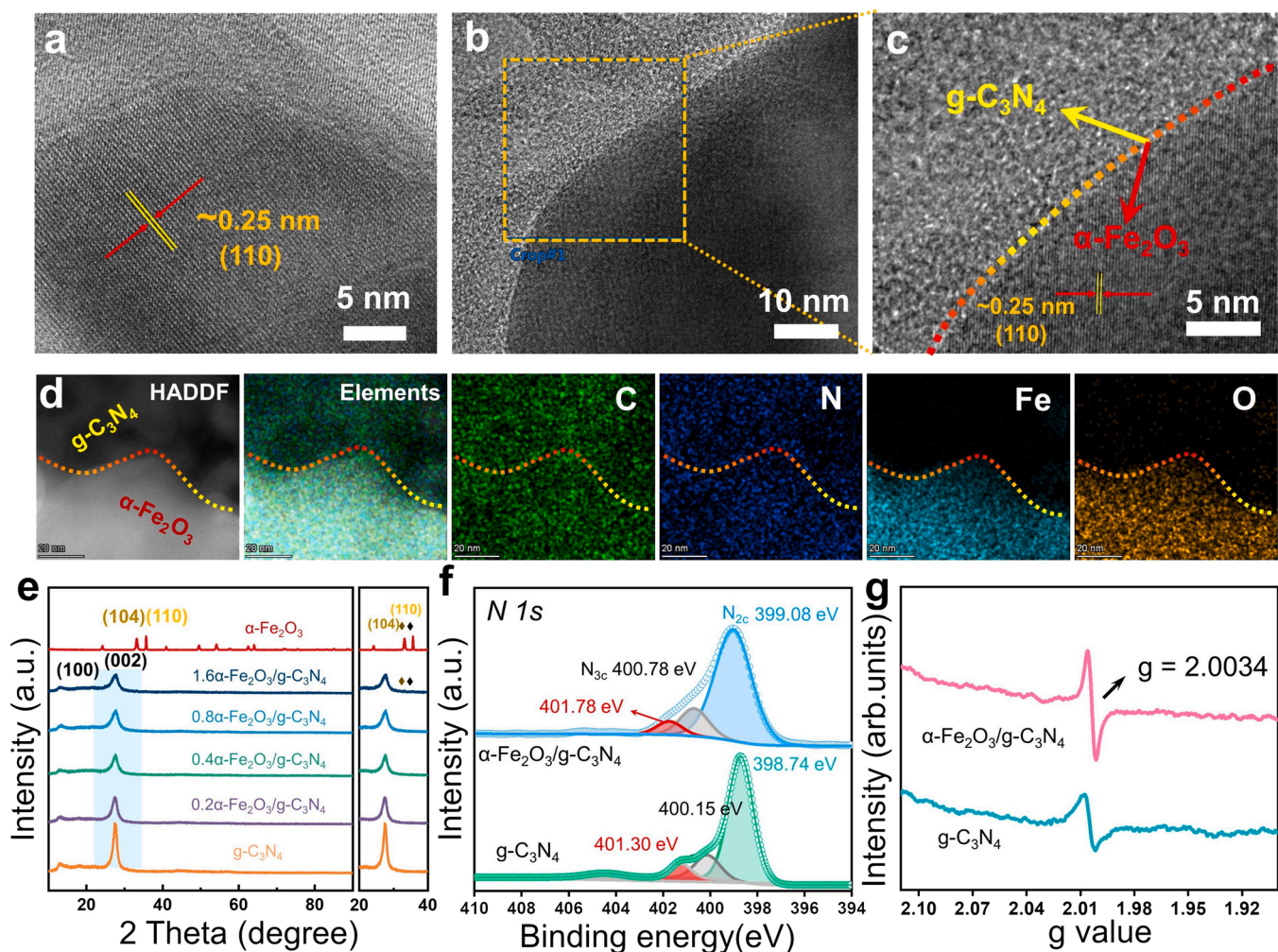
Fig. 1. (a) HRTEM image of α-Fe$_2$O$_3$. (b) TEM and (c) HRTEM images of α-Fe$_2$O$_3$/g-C$_3$N$_4$ composites. (d) HAADF-STEM image and the corresponding EDS element (C, N, Fe, O) mappings of the α-Fe$_2$O$_3$/g-C$_3$N$_4$. (e) XRD patterns. (f) N 1 s XPS spectra and (g) EPR spectra of g-C$_3$N$_4$ and α-Fe$_2$O$_3$/g-C$_3$N$_4$ composites.

Significantly, the sharp interfaces between α-Fe$_2$O$_3$ and g-C$_3$N$_4$ can be clearly observed (Fig. 1b-c), which indicates that the α-Fe$_2$O$_3$/g-C$_3$N$_4$ heterojunction has been successfully constructed. The corresponding EDS element (C, N, Fe, O) mappings of α-Fe$_2$O$_3$/g-C$_3$N$_4$ also confirms the intimate contact between two phases (Fig. 1d). Moreover, X-ray diffraction (XRD) and Fourier transform infrared spectroscopy (FT-IR) were performed to probe the crystalline texture of all samples (Fig. 1e and Fig. S7). For pristine g-C$_3$N$_4$, there are two typical diffraction peaks at 13.1°and 27.4°, representing the (100) interplanar packing of s-triazine ring units and (002) the interlayer stacking of g-C$_3$N$_4$ nanosheets, respectively [26,27]. In sharp contrast, although these two characteristic peaks appeared in all α-Fe$_2$O$_3$/g-C$_3$N$_4$ heterojunction samples, their intensity decreases significantly with the increase of α-Fe$_2$O$_3$ content, which indicates that the introduction of α-Fe$_2$O$_3$ promotes the formation of defects in g-C$_3$N$_4$ structural units and the weakened layered stacking. Accordingly, the α-Fe$_2$O$_3$/g-C$_3$N$_4$ heterojunction exhibits a larger specific surface area than α-Fe$_2$O$_3$ and pristine g-C$_3$N$_4$ (Fig. S8 and Table S1), which indicates that it can provide more active sites for the activation of molecular oxygen, thereby enhancing the photocatalytic performance. Meanwhile, the (104) and (110) peak intensities of α-Fe$_2$O$_3$ are gradually strengthened with the increase of α-Fe$_2$O$_3$ content, which further evidence the assembly of α-Fe$_2$O$_3$ and g-C$_3$N$_4$. All above results illustrate that α-Fe$_2$O$_3$/g-C$_3$N$_4$ hybrids was successfully synthesized and the formation of tight heterointerfaces would favors the transfer of photogenerated carriers.

To further confirm the existence of nitrogen defects on α-Fe$_2$O$_3$/g-C$_3$N$_4$ heterojunction, element analysis (EA), X-ray photoelectron spectroscopy (XPS) and electron paramagnetic resonance (EPR) spectra were carried out. In contrast with pristine g-C$_3$N$_4$, the EA result of α-Fe$_2$O$_3$/g-C$_3$N$_4$ heterostructures show that the C/N atomic ratio increases (from 0.55 to 0.69) with the increase of α-Fe$_2$O$_3$ content (Table S2), demonstrating the coupling of α-Fe$_2$O$_3$ promotes the formation of nitrogen defects in prepared compound material. Compared with pristine phase g-C$_3$N$_4$, the enhanced EPR signal at g = 2.0034 is observed in α-Fe$_2$O$_3$/g-C$_3$N$_4$ heterostructures (Fig. 1g), which is caused by the unpaired electron on the aromatic ring carbon atom [28]. In addition, Fig. 1f shows the high-resolution N 1 s spectra of g-C$_3$N$_4$ and α-Fe$_2$O$_3$/g-C$_3$N$_4$ heterojunction. The sharp N 1 s spectrum of g-C$_3$N$_4$ can be deconvoluted into three peaks centered at 398.74 eV, 400.15 eV and 401.30 eV, which can be assigned to C-N = C, N-C$_3$ and C-N-H [18,29]. Moreover, these energy bands of N related moieties are positively shifted about 0.34 eV after forming heterointerface, suggesting the intense chemical interaction is presented between g-C$_3$N$_4$ and α-Fe$_2$O$_3$ in α-Fe$_2$O$_3$/g-C$_3$N$_4$ heterojunction. Notably, the ratio between C-N = C and N-C$_3$ decreased from 5.02 to 4.06, implying that the defects are preferentially engineered at N$_{2c}$ site. As observed in Fig. S9, the C 1 s high-resolution XPS spectrum in g-C$_3$N$_4$ is divided into 288.16 eV, 286.24 eV and 284.60 eV, which are stemmed from N-C=N, N = C-N and C-C, respectively [30]. Whereas the intensity of the N = CH-N peak increases significantly with the loss of N$_{2c}$ atoms in α-Fe$_2$O$_3$/g-C$_3$N$_4$ heterojunction. Moreover, two characteristic peaks located in 724.28 eV and 710.48 eV in Fig. S10a were attributed to Fe $2p_{1/2}$ and Fe $2p_{3/2}$ of Fe^{3+}, respectively, which

further confirms the existence of α-Fe$_2$O$_3$ in heterojunction. Fig. S10b shows the high-resolution O1s spectra of α-Fe$_2$O$_3$/g-C$_3$N$_4$. It can be deconvoluted into two peaks at 529.66 eV and 532.47 eV, corresponding to lattice oxygen (Fe-O) of α-Fe$_2$O$_3$ and the adsorbed hydroxyl group (-OH) on the surface. As above mentioned, it is proved that there are abundant nitrogen defects in our successfully designed α-Fe$_2$O$_3$/g-C$_3$N$_4$ heterojunction surface, which is expected to provide more active centers for molecular oxygen adsorption and electron trapping.

3.2. Photocatalytic oxygen activation performance

The successful design of α-Fe$_2$O$_3$/g-C$_3$N$_4$ composites allowed us to first explore their molecular oxygen activation activity with 3,3′,5,5′-tetramethylbenzidine (TMB) as an indicator molecule. Confirmed by the time-dependent absorption spectra of TMB oxidation, the α-Fe$_2$O$_3$/g-C$_3$N$_4$ composite displays the highest oxygen activation ability (Fig. 2a). As illustrated in Fig. 2b, oxidation rates of TMB by the synthesized photocatalyst are significantly different in various atmospheres (O$_2$, air, and N$_2$), indicating that the ROS are converted from oxygen. To elucidate the main type of reactive species that was generated in α-Fe$_2$O$_3$/g-

C$_3$N$_4$ system, p-benzoquinone, tert-butyl alcohol, EDTA-2Na and carotene were added into the reaction solution to specifically suppress the production of O$_2^{\bullet-}$, ·OH, h$^+$ and ^{1}O$_2$, respectively. As depicted in Fig. 2c, the p-benzoquinone, tert-butyl alcohol and carotene dramatically decrease TMB oxidation. It is suggested that the abundant ROS of O$_2^{\bullet-}$, ·OH and ^{1}O$_2$ are generated in the photocatalytic system of α-Fe$_2$O$_3$/g-C$_3$N$_4$, which may be derived from the different reaction thermodynamic conditions of band structures staggered alignment of α-Fe$_2$O$_3$ and g-C$_3$N$_4$.

Subsequently, electron paramagnetic resonance (EPR) test was performed, which provided strong evidence for the formation of transient radical inter-mediates. DMPO was used as a trapping agent to stabilize the O$_2^{\bullet-}$ and ·OH produced by the photocatalytic reaction in methanol (DMPO-O$_2^{\bullet-}$) and aqueous solution (DMPO-·OH). For pristine g-C$_3$N$_4$ catalytic system, only DMPO-O$_2^{\bullet-}$ signal is detected (Fig. 2d). While, in the pure α-Fe$_2$O$_3$ catalytic system, only four characteristic peaks of DMPO-·OH signal (the intensities were 1:2:2:1) are detected (Fig. 2e). Notably, the signals attributed to DMPO-O$_2^{\bullet-}$ and DMPO-·OH are clearly observed in the α-Fe$_2$O$_3$/g-C$_3$N$_4$ catalytic system, and the intensity is significantly enhanced, which strongly confirms that the α-Fe$_2$O$_3$/g-
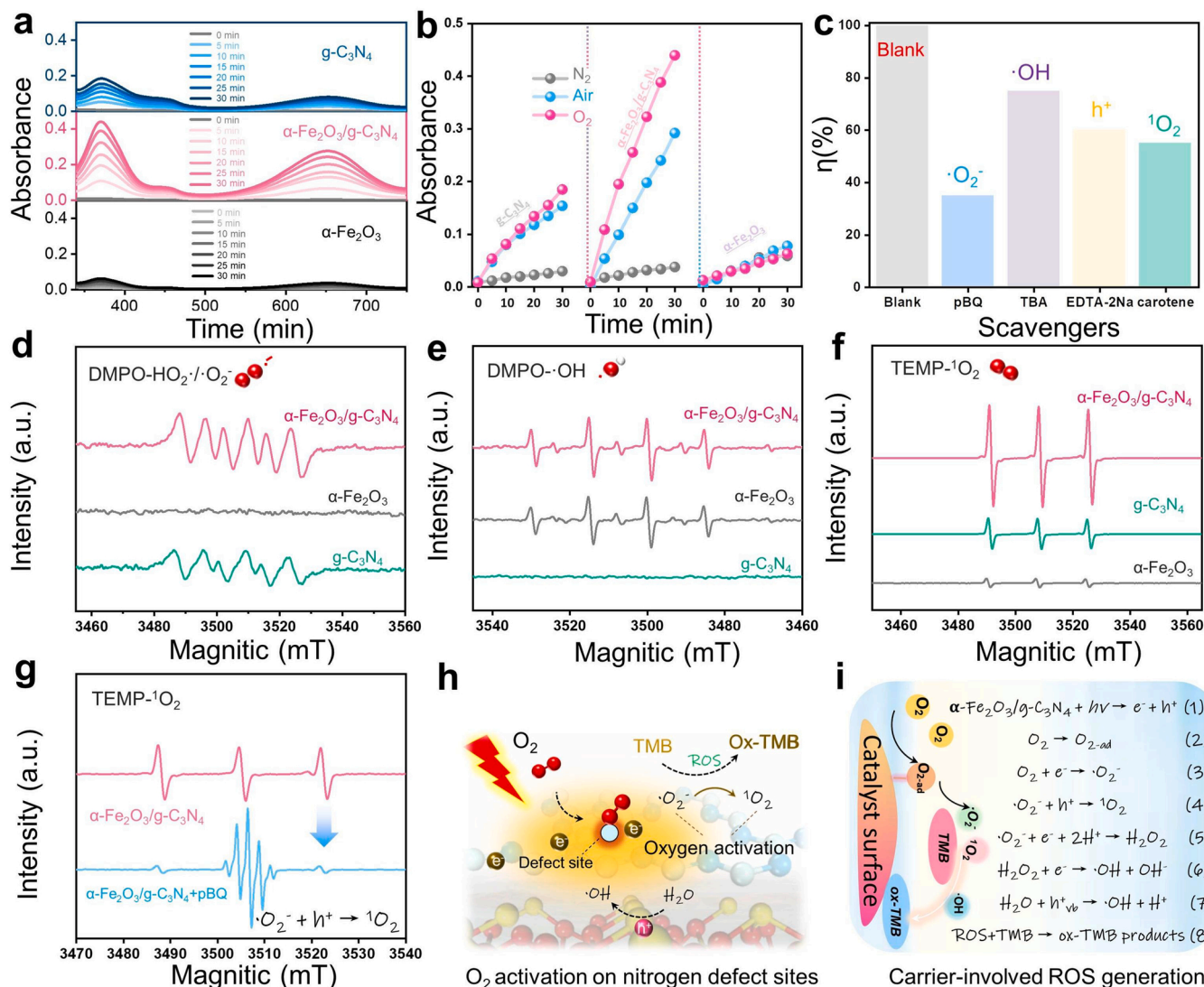
Fig. 2. (a) Time-dependent absorption spectra, and (b) the absorbance peak monitored for the product at 370 nm vs reaction time under different gas conditions of g-C$_3$N$_4$, α-Fe$_2$O$_3$ and α-Fe$_2$O$_3$/g-C$_3$N$_4$. (c) Absorbance change over α-Fe$_2$O$_3$/g-C$_3$N$_4$ at 370 nm with different scavengers of TMB oxidation. (d-e) DMPO spin-trapping EPR spectra of g-C$_3$N$_4$, α-Fe$_2$O$_3$ and α-Fe$_2$O$_3$/g-C$_3$N$_4$ (in aqueous for DMPO-•OH, in methanol for DMPO-•O$_2$). (f) TEMP spin-trapping EPR spectra for ^{1}O$_2$. (g) EPR spectra for the detection of ^{1}O$_2$ in the presence of TEMP and p-benzoquinone. (h) Schematic diagram of molecular oxygen activation of α-Fe$_2$O$_3$/g-C$_3$N$_4$ heterojunction. (i) The scheme for the carrier-involved ROS generation process.

C$_3$N$_4$ hybrid forms an all-solid Z-scheme structure rather than a p-n heterojunction. In addition, singlet oxygen is also identified by EPR spectrum. As illustrated in Fig. 2f, the heterojunction system exhibits obvious enhancement of TEMP-^{1}O$_2$ relative to the pristine α-Fe$_2$O$_3$ and g-C$_3$N$_4$ system. Furthermore, the source analysis of singlet oxygen produced in heterojunction system was carried out, as shown in Fig. 2g. The signal of ^{1}O$_2$ in the heterojunction system is obviously weakened with the quenching of O$_2^{\bullet-}$, indicating that most of the ^{1}O$_2$ comes from the oxidation of O$_2^{\bullet-}$ by h$^+$ [31], rather than a simple energy transfer. Based on the study of active species mentioned above, the possible mechanism of photocatalytic activation of molecular oxygen by α-Fe$_2$O$_3$/g-C$_3$N$_4$ was proposed in Fig. 2h. Briefly, electrons originating from visible light-irradiated are transferred to the surface of the catalyst, which can activate the O$_2$ adsorbed on the g-C$_3$N$_4$ defects, resulting in a large amount of O$_2^{\bullet-}$. Meanwhile, ^{1}O$_2$ can be produced by the oxidation of O$_2^{\bullet-}$ by h$^+$. Therefore, O$_2^{\bullet-}$ and ^{1}O$_2$ are the activation products of oxygen by photogenerated electrons at the defective surfaces. Benefiting from abundant ROS generation, α-Fe$_2$O$_3$/g-C$_3$N$_4$ system exhibits excellent properties for carrier-involved molecular oxygen activation (Fig. 2i).

3.3. Mechanism of enhanced photocatalytic oxygen activation

We subsequently sought to clarify how the construction of defective heterojunction endow g-C$_3$N$_4$ with superior photocatalytic oxygen activation ability. In this context, charge separation and transfer, light absorption, and surface oxygen activation were characterized in detail. To elucidate the charge-carrier dynamics of heterojunction, a series of photoelectrochemical characterization and steady-state photoluminescence (PL) emission spectra were first performed. As illustrated in Fig. 3a, dramatic PL quenching occurs on the α-Fe$_2$O$_3$/g-C$_3$N$_4$ relative to pristine g-C$_3$N$_4$, indicating that the intrinsic radiative recombination of photoexcited electron-hole pairs in α-Fe$_2$O$_3$ and g-C$_3$N$_4$ has been

significantly inhibited by the construction of Z-scheme heterostructures, and the synergistic effect of heterojunction and defects promotes charge transfer [32]. Evidently, the time-resolved transient PL decay spectra of heterojunction shows a longer carriers average PL lifetime (9.18 ns) with respect to the g-C$_3$N$_4$ (7.43 ns) and α-Fe$_2$O$_3$ (2.68 ns), confirming more photogenerated electrons can participate in molecular oxygen activation than α-Fe$_2$O$_3$ and g-C$_3$N$_4$ (Fig. 3b and Table S3). This can be further corroborated by the photocurrent responses, the photocurrent response intensity of α-Fe$_2$O$_3$/g-C$_3$N$_4$ is 8.8 and 2.3 times higher than α-Fe$_2$O$_3$ and g-C$_3$N$_4$, respectively (Fig. 3c), indicating that separation efficiency of charge carriers is greatly increased in the α-Fe$_2$O$_3$/g-C$_3$N$_4$ heterojunction. In addition, electrochemical impedance spectroscopy (EIS) is shown in Fig. 3d. The results show that α-Fe$_2$O$_3$/g-C$_3$N$_4$ has a smaller semicircle diameter and lower R$_t$ value (1.28 × 10^{12} Ω) than g-C$_3$N$_4$ (7.64 × 10^{18} Ω), which verifies the significant improvement of interfacial charge transfer resistance. Similarly, the carrier density (N$_d$) for α-Fe$_2$O$_3$/g-C$_3$N$_4$ = 1.86 × 10^{18} cm^{-3} increased compared to g-C$_3$N$_4$ = 9.82 × 10^{17} cm^{-3}, as determined from the Mott-Schottky plot (Fig. S11) [33], which provide more evidence for the above results.

Leveraging nitrogen vacancy as an oxygen adsorption site has been demonstrated on the surface of g-C$_3$N$_4$-based photocatalysts [17,18]. Therefore, we studied the absorption of O$_2$ through O$_2$-TPD. As shown in Fig. 4a, compared with pristine g-C$_3$N$_4$, the heterojunction sample shows a stronger desorption peak at 155 °C, implying that the nitrogen vacancy on g-C$_3$N$_4$ surface of α-Fe$_2$O$_3$/g-C$_3$N$_4$ heterojunction has excellent oxygen adsorption capacity and can provide a large number of absorption sites to activate O$_2$ [34]. In addition, the optical properties of g-C$_3$N$_4$, α-Fe$_2$O$_3$ and α-Fe$_2$O$_3$/g-C$_3$N$_4$ were determined by UV-Vis diffuse reflectance spectroscopy (DRS). It is observed that absorption edge of α-Fe$_2$O$_3$/g-C$_3$N$_4$ exhibit a redshift in compared with the pristine g-C$_3$N$_4$, along with a change in the sample color from yellow to pale pink (insets in Fig. 4b). As determined from the transformed Kubelka-Munk function
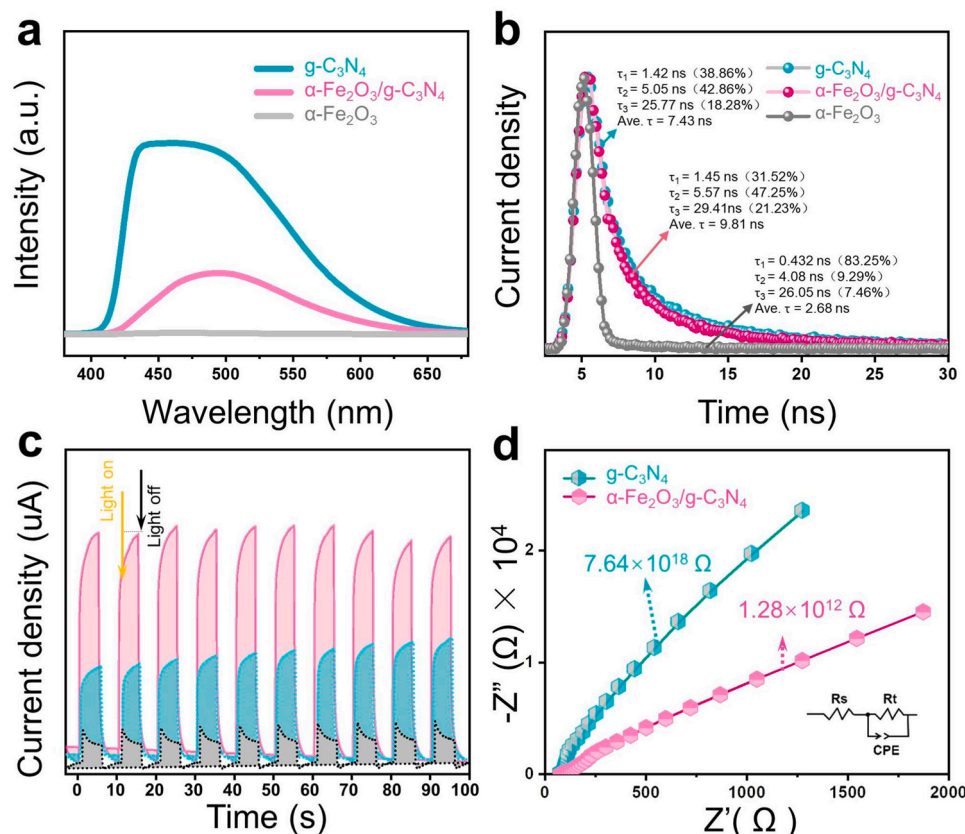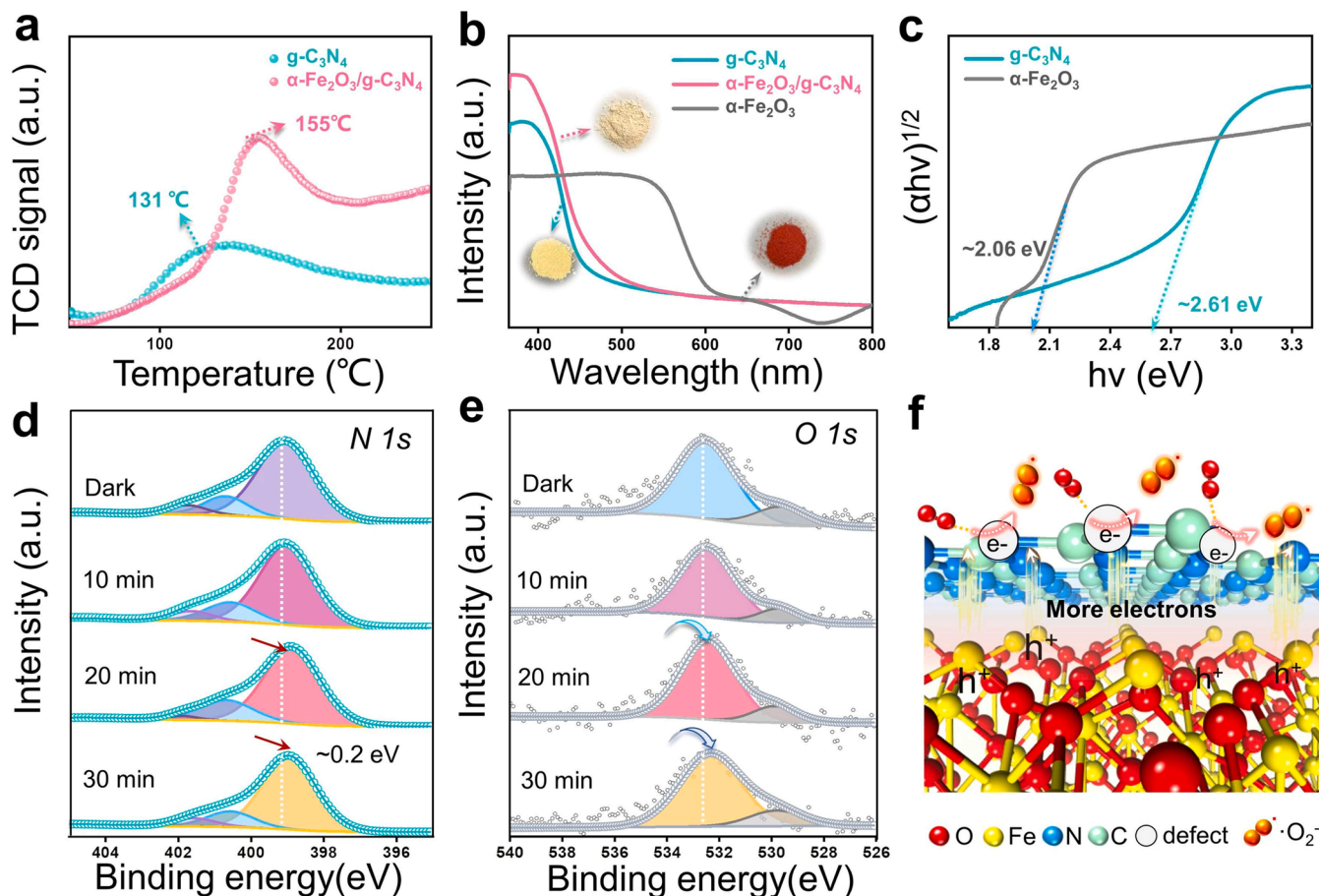

Fig. 3. (a) Steady-state PL spectra, (b) Time-resolved PL spectra, (c) photocurrent responses, (d) EIS Nyquist plots of g-C$_3$N$_4$, α-Fe$_2$O$_3$ and α-Fe$_2$O$_3$/g-C$_3$N$_4$.

Fig. 4. (a) O$_2$-TPD signal of g-C$_3$N$_4$ and α-Fe$_2$O$_3$/g-C$_3$N$_4$. (b) UV–vis diffuse reflectance spectra of g-C$_3$N$_4$, α-Fe$_2$O$_3$ and α-Fe$_2$O$_3$/g-C$_3$N$_4$. (c) The band gaps that estimated by a related curves of $(\alpha h\nu)^{1/2}$. *In-situ* synchronous illumination XPS spectra of (d) N 1 s and (e) O 1 s of α-Fe$_2$O$_3$/g-C$_3$N$_4$ under oxygen feeding for certain time. (f) Schematic illustration of the electron transfer in α-Fe$_2$O$_3$/g-C$_3$N$_4$ under visible light irradiation.

[35], the bandgaps (Eg) of g-C$_3$N$_4$ and α-Fe$_2$O$_3$ are calculated to be 2.61 and 2.06 eV, respectively (Fig. 4c). As revealed by the VB XPS spectra, the maximum valence bands of g-C$_3$N$_4$ and α-Fe$_2$O$_3$ are 1.49 and 2.51 eV, respectively (Fig. S12).

To fully reveal the mechanism of the improvement of photocatalytic activity, especially with the key role of interfacial charge transfer direction between g-C$_3$N$_4$ and α-Fe$_2$O$_3$, in-situ synchronous illumination XPS and density function theory (DFT) were studied. As displayed in Fig. 4d, N 1 s spectra of heterojunction sample shift towards the direction of lower binding energy under visible light irradiation and O$_2$ ambient, indicating that photogenerated electrons transfer from α-Fe$_2$O$_3$

to g-C$_3$N$_4$ across the interface, providing direct evidence for the Z-shaped electron transfer route. Moreover, the O 1 s spectra of α-Fe$_2$O$_3$/g-C$_3$N$_4$ obviously shift towards lower binding energy (Fig. 4e), suggesting that the absorbed O$_2$ molecule accepts electrons, and the constructed Z-scheme heterojunction will effectively inject electrons into the adsorbed O$_2$ molecules on the defect sites. Since the carbon atoms dangling around the nitrogen defects continuously donate electrons to the anti-bonding orbital of adsorbed O$_2$, the C 1 s spectrum shifts significantly to the higher binding energy by about 0.3 eV (Fig. S13). Moreover, DFT calculation was adopted to explore the work function which would be helpful to understand the driving force of the Z-scheme electron transfer
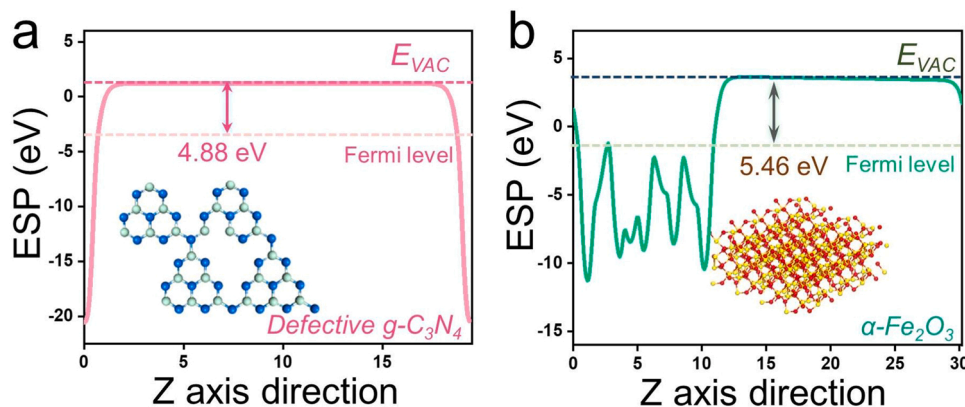
Fig. 5. Calculated work functions for (a) defective g-C$_3$N$_4$ (001) and (b) α-Fe$_2$O$_3$ (001) surfaces, respectively.

mechanism. As shown in Fig. 5, the work functions (Φ) of defective g-C₃N₄ (001) and α-Fe₂O₃ (001) are calculated to be 4.48 and 5.46 eV, respectively. Accordingly, the Fermi level of defect g-C₃N₄ (−4.48 eV) is higher than that of α-Fe₂O₃ (−5.46 eV). When two phases are in intimate contact to form a heterojunction in darkness, the difference of E_f promotes the spontaneous rearrangement of charge, and the charge in g-C₃N₄ continues to transfer to α-Fe₂O₃ until E_f reaches equilibrium [36]. Finally, a built-in electric field is formed at the heterogeneous interface of α-Fe₂O₃/g-C₃N₄ (Fig. S14), which is conducive to driving the directional migration of carriers through the Z-scheme transfer path, and provides a large number of photogenerated carriers with strong redox capabilities for photocatalytic reaction.

With a comprehensive consideration of the band structures (Fig. 4c and Fig. S12), in-situ synchronous illumination XPS and the DFT calculations, a typical direct Z-scheme structure, rather than a p-n heterojunction (Fig. S15), charge-transfer pathway is proposed for the α-Fe₂O₃/g-C₃N₄ composite, which can also be strongly supported by the EPR results (Fig. 2d and e). Specifically, the α-Fe₂O₃ semiconductor can be excited by visible light, causing electrons to migrate from the VB to the CB position, while the valence band leaves photogenerated h⁺ accordingly. Our synthesis approach creates an intimate interface between α-Fe₂O₃ and g-C₃N₄, in which the photoexcited electrons at the CB of the α-Fe₂O₃ and the photoexcited holes at the VB of the g-C₃N₄ would be rapidly recombined at the heterostructure interfaces, while the photoexcited holes and electrons retained at VB of α-Fe₂O₃ and the CB of g-C₃N₄, respectively (Fig. 4f). Subsequently, the electrons in the g-C₃N₄ CB can be effectively trapped by the surface nitrogen defects, thus driving the oxygen reduction reactions to produce •O₂ (E⁰ (O₂/•O₂⁻) = −0.33 V) [37]. In addition, the potential of H₂O/•OH (E⁰ (H₂O/•OH) = 2.34 V) is more higher than the VB of α-Fe₂O₃, which will oxidize H₂O or OH⁻ into •OH (H₂O + h_{vb}^+ → •OH + H⁺ or OH⁻ + h_{vb}^+ → •OH). Among them, as the adsorption center of oxygen and electron capture center, nitrogen defects establish a sequential photoelectron transfer channels

in the heterojunction catalyst, so that the photogenerated electrons are continuously transferred to the adsorbed oxygen molecules through the defect sites to participate in the activation of oxygen. Due to this spatial separation of oxidation and reduction sites, the recombination efficiency of electrons and holes is significantly inhibited, and the maximum carrier utilization efficiency is achieved. Therefore, the defect-mediated Z-scheme electron transfer path significantly improves photocatalytic activate oxygen performance.

3.4. Photocatalytic degradation performance

In light of the encouraging molecular oxygen activation properties, taking TC as a typical antibiotic pollutant, we further explored the photocatalytic oxidation ability of defect-mediated α-Fe₂O₃/g-C₃N₄ heterojunction under visible light (λ > 420 nm). As shown in Fig. 6a, α-Fe₂O₃/g-C₃N₄ heterojunction has a more notable photocatalytic oxidation ability than pristine g-C₃N₄ and α-Fe₂O₃. Specifically, pristine g-C₃N₄ and α-Fe₂O₃ presents poor photocatalytic degradation performance of TC due to their serious electron-hole pair recombination, and only 46.72% and 20.59% degradation efficiency can be achieved at 60 min. In contrast, the defect-mediated α-Fe₂O₃/g-C₃N₄ heterojunction shows a significantly improved TC removal efficiency, and nearly 80% of pollutants are removed at reaction time for 20 min and 95% at 60 min. As a control, the concentration of pollutants remains almost unchanged in the absence of photocatalysts, suggesting that TC is stable under visible light, and the degradation performance is exclusively derived from our synthesized catalysts. For a quantitative comparison of kinetics, the pseudo-first-order rate constant (k) and correlation coefficient were calculated (Fig. 6b). It can be seen that the k value of α-Fe₂O₃/g-C₃N₄ heterojunction is the highest (0.05304 min⁻¹) relative to the g-C₃N₄ (0.01117 min⁻¹) and α-Fe₂O₃ (0.00441 min⁻¹). These results suggest that the α-Fe₂O₃/g-C₃N₄ heterojunction has excellent photocatalytic ability to activate oxygen, and the resulting highly
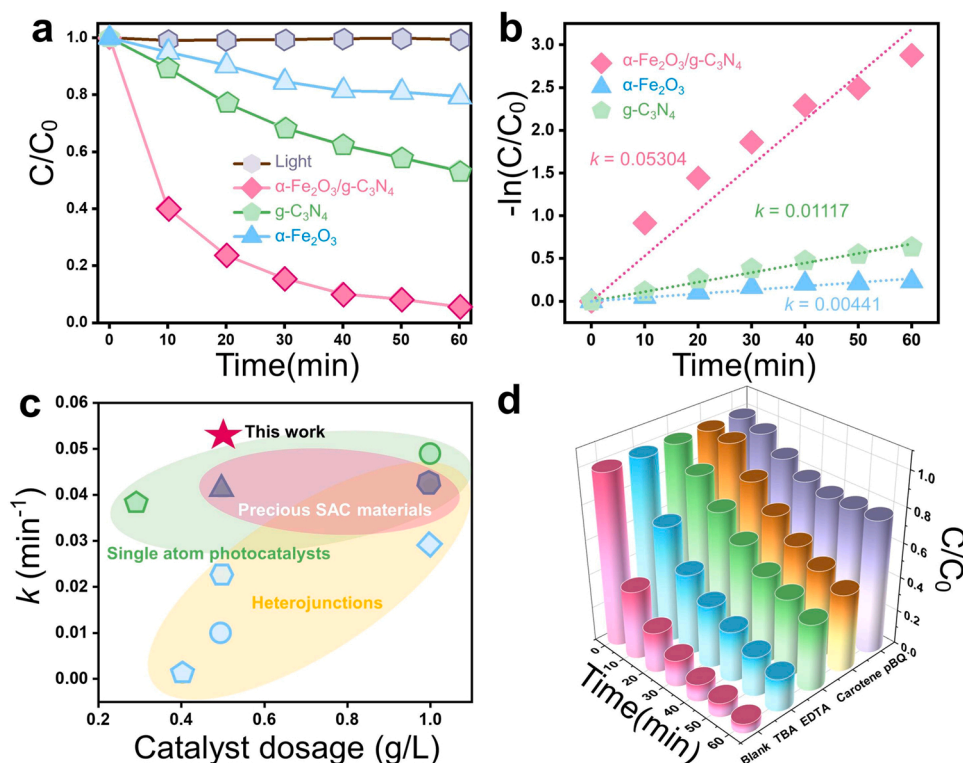
Fig. 6. (a) Photocatalytic degradation efficiency of TC (20 mg/L) over different samples under visible light irradiation (λ > 420 nm). (b) Pseudo-first-order kinetic fitting curves and the corresponding kinetic constants. (c) Comparison of *k* values of several photocatalytic materials for TC removal. (d) The photocatalytic degradation efficiencies of TC (20 mg/L) by α-Fe₂O₃/g-C₃N₄ with different scavengers.

reactive ROS can efficiently degrade organic pollutants. As shown in Fig. 6c and Table S4, the photocatalytic degradation activity α-Fe$_2$O$_3$/g-C$_3$N$_4$ heterojunction is higher than most of other g-C$_3$N$_4$-based photocatalysts reported in recent years, even some precious metal single atom catalysts, which shows the superiority of α-Fe$_2$O$_3$/g-C$_3$N$_4$ photocatalyst in water purification.

Based on the Z-shaped electron transfer route, we know that abundant superoxide radicals and hydroxyl radicals would be produced in α-Fe$_2$O$_3$/g-C$_3$N$_4$ heterojunction photocatalysis system. To understand the key factors of photocatalytic degradation of TC, trapping experiments were conducted to detect the possible transient radical

intermediates. As depicted in Fig. 6d, the adding *p*-benzoquinone, carotene, tert-butyl alcohol, EDTA-2Na scavengers, the degradation efficiency of α-Fe$_2$O$_3$/g-C$_3$N$_4$ is restrained in different degrees. Remarkedly, the degradation efficiency is drastically inhibited by *p*-benzoquinone, revealing that the production of •O$_2^-$ by activated oxygen is the major step in the degradation of TC. In addition, according to TOC analysis (Fig. S16), after 3 h of visible light irradiation, the mineralization rate of α-Fe$_2$O$_3$/g-C$_3$N$_4$ to TC reached 32.5%, indicating that α-Fe$_2$O$_3$/g-C$_3$N$_4$ could degrade tetracycline into H$_2$O, CO$_2$ and small molecular compounds. The above results confirm that Z-scheme heterojunction has excellent molecular oxygen activation ability and has a
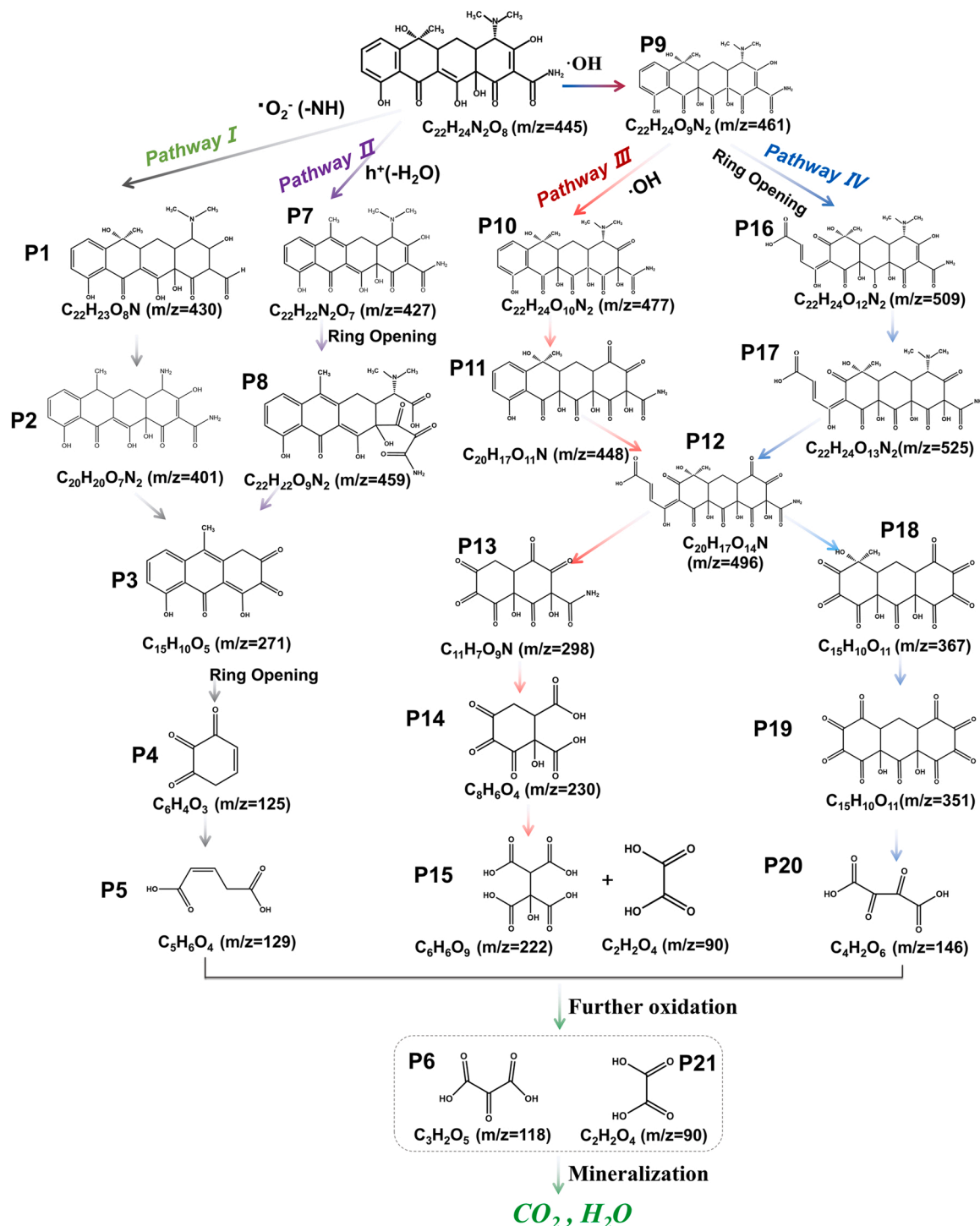

Fig. 7. Possible catalytic degradation pathway of TC in photocatalytic oxidation process.

broad application prospect in water treatment.

To further understand the degradation pathway and mechanism of TC degradation in α-Fe$_2$O$_3$/g-C$_3$N$_4$ system, the intermediate products were detected by the liquid chromatography coupled with mass spectrometry (LC-MS), and the results shown in Table S5. From the detected 21 intermediates and related reports, Fig. 7 proposes four possible pathways for photocatalytic degradation of TC by α-Fe$_2$O$_3$/g-C$_3$N$_4$ heterojunction. The original signal of mass/charge is $m/z = 445$, which represents the complete structure of TC molecule. Considering that the defect-mediated heterojunction system has good molecular oxygen activation ability, it will produce abundant active •O$_2^-$ in the photocatalysis process. In path I, the amino group of TC molecule is removed under the reaction of •O$_2^-$ to form the primary intermediate product P1 with $m/z = 430$, and transformed to the intermediate of $m/z = 401$ via the cleavage of group -NH. After further ring-opening and other reactions, the small molecular reactant P5 with $m/z = 129$ is finally formed. Moreover, the original TC molecule also can be decomposed to P7 ($m/z = 427$) via dehydration, and transformed to the product P8 ($m/z = 459$) under ROS attack (path II). Subsequently, these secondary intermediates are also oxidized to produce ring-opening small molecular compounds, including P3 ($m/z = 271$), P4 ($m/z = 125$) and P5 ($m/z = 129$). In addition, hydroxyl radicals also play an critical role in the degradation of tetracycline. Specifically, double bond, phenolic group and amino group in TC have high electron density, which are easy to be attacked by hydroxyl radical in the process of degradation. The potential of H$_2$O/•OH (E^0 (H$_2$O/•OH) = 2.34 V) was higher than the VB of α-Fe$_2$O$_3$ in α-Fe$_2$O$_3$/g-C$_3$N$_4$ heterojunction, which will oxidize H$_2$O or OH$^-$ into •OH. Evidently, the detected P9 ($m/z = 461$) is ascribed to related hydroxylated product. Subsequently, the primary intermediate P9 can be further oxidized into two potential secondary intermediates by •OH attacks at different double bond locations (P10 and P16), with a charge-mass ratio of 477 and 509, respectively (path III and path IV). These secondary intermediates are further oxidized and gradually form small molecular organic compounds, i. e., P6 (($m/z = 118$), P15 ($m/z = 222$), P20 ($m/z = 146$) and P21 ($m/z = 90$). Eventually, these ring-

opening products are converted into H$_2$O and CO$_2$.

Furthermore, computational toxicology method was applied to analyze and predict the aquatic toxicity of TC and its transformation products in the process of photocatalysis, according to the structural formulas of the above intermediates [38]. As exhibited in Fig. 8 and Table S6, the acute toxicity was reckoned as LC$_{50}$ for fish and daphnia, and EC$_{50}$ for green algae, and these results are 27.1, 2.9 and 3.3 mg/L for original TC, respectively. Chronic toxicity values (ChV) of TC are 7.3, 0.6, and 0.8 mg/L for fish, daphnia, and green algae, respectively. This shows that TC is classified as a highly toxic compound to aquatic organisms according to the European Union criteria and Chinese hazard evaluation guidelines of new chemical substances (HJ/T 154–2004). For the chronic and acute toxicities of degradation products, most intermediates are harmless to three aquatic organisms. Encouragingly, among the four reaction pathways, we found that the chronic and acute toxicity decrease gradually with the progress of photocatalytic degradation. As depicted in Fig. 8 and Fig. S17, part of toxic and harmful intermediates will be generated in the TC degradation process using the α-Fe$_2$O$_3$/g-C$_3$N$_4$ catalyst, which can be further degraded by abundant active oxygen species and converted into CO$_2$ and H$_2$O in a certain period of time. Hence, the α-Fe$_2$O$_3$/g-C$_3$N$_4$ system has an effective detoxification effect on TC, which further confirms its potential advantages in water treatment.

4. Conclusions

In summary, we have successfully constructed a novel Z-scheme α-Fe$_2$O$_3$/g-C$_3$N$_4$ heterojunction with abundant N defects for photocatalytic molecular O$_2$ activation. Extensive characterizations reveal that the strong interfacial interaction was present between g-C$_3$N$_4$ and α-Fe$_2$O$_3$, which significantly enhanced charge-separation and transfer efficiency. The unique Z scheme electron transfer route provides a large number of photogenerated carriers with strong redox capabilities for molecular oxygen activation and ensures the thermodynamic conditions for •OH and •O$_2^-$ generation. Meanwhile, the N defects in the g-C$_3$N$_4$ can
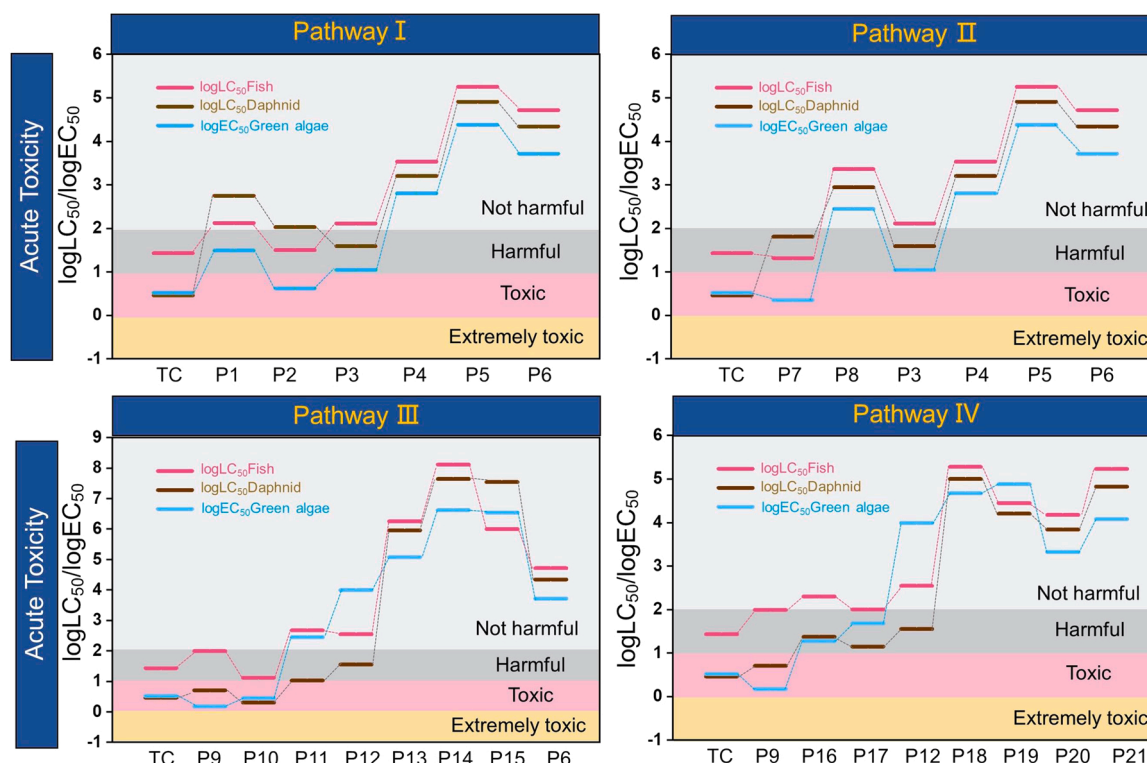

Fig. 8. Acute toxicity evolution of TC and its degradation intermediates toward three aquatic organisms using EPI Suite software with ECOSAR program.

serve as an electron sink as well as O_2 adsorption sites, which facilitate the adsorption of O_2 and greatly promote photogenerated electrons transferred from $\alpha\text{-}Fe_2O_3/g\text{-}C_3N_4$ heterojunction to the adsorbed O_2 molecules with N_v as a bridge. Benefiting from the accelerated transfer and of separation of photoexcited carriers, the defect-mediated $\alpha\text{-}Fe_2O_3/g\text{-}C_3N_4$ heterojunction presents excellent catalytic performance for molecular oxygen activation activity under visible light irradiation ($\lambda > 420$ nm). As a result, an exceptional boosted photocatalytic performance for TC degradation by $\alpha\text{-}Fe_2O_3/g\text{-}C_3N_4$ heterojunction is observed up to 4.7 and 12 times over the pristine $g\text{-}C_3N_4$ and $\alpha\text{-}Fe_2O_3$, respectively. Moreover, the LC-MS and ECOSAR prediction prove the $\alpha\text{-}Fe_2O_3/g\text{-}C_3N_4$ composites exhibit effective detoxification effect on TC. This work proposes a new approach to accelerate the activation of molecular oxygen and a practical way for the application of photocatalysis in practical waste water treatment.

CRediT authorship contribution statement

Lina Su: Investigation, Writing – original draft, Formal analysis, Funding acquisition. **Pengfei Wang:** Supervision, Funding acquisition, Writing – review & editing. **Mingmei Li**: Methodology. **Zhiyong Zhao**: Investigation. **Yi Li**: Supervision, Funding acquisition, Writing – review & editing. **Sihui Zhan**: Supervision, Funding acquisition.

Declaration of Competing Interest

The authors declare that they have no known competing financial interests or personal relationships that could have appeared to influence the work reported in this paper.

Data Availability

Data will be made available on request.

Acknowledgements

Appendix A. Supporting information

Supplementary data associated with this article can be found in the online version at doi:10.1016/j.apcatb.2023.122890.

References

[1] T.U. Berendonk, C.M. Manaia, C. Merlin, D. Fatta-Kassinos, E. Cytryn, F. Walsh, H. Buergmann, H. Sorum, M. Norstrom, M.-N. Pons, N. Kreuzinger, P. Huovinen, S. Stefani, T. Schwartz, V. Kisand, F. Baquero, J. Luis Martinez, Tackling antibiotic resistance: the environmental framework, Nat. Rev. Microbiol. 13 (2015) 310–317, https://doi.org/10.1038/nrmicro3439.

[2] X. Duan, H. Sun, Z. Shao, S. Wang, Nonradical reactions in environmental remediation processes: uncertainty and challenges, Appl. Catal. B: Environ. 224 (2018) 973–982, https://doi.org/10.1016/j.apcatb.2017.11.051.

[3] H. Guo, C.G. Niu, C.-Y. Feng, C. Liang, X.-J. Wen, Y. Yang, H.-Y. Liu, L. Li, L.-S. Lin, Steering exciton dissociation and charge migration in green synthetic oxygen-substituted ultrathin porous graphitic carbon nitride for boosted photocatalytic reactive oxygen species generation, Chem. Eng. J. 385 (2020), 123919, https://doi.org/10.1016/j.cej.2019.123919.

[4] T. Jia, J. Wu, J. Song, Q. Liu, J. Wang, Y. Qi, P. He, X. Qi, L. Yang, P. Zhao, In situ self-growing 3D hierarchical BiOBr/BiOIO3 Z-scheme heterojunction with rich oxygen vacancies and iodine ions as carriers transfer dual-channels for enhanced photocatalytic activity, Chem. Eng. J. 396 (2020), 125258, https://doi.org/10.1016/j.cej.2020.125258.

[5] M. Li, P. Wang, Z. Ji, Z. Zhou, Y. Xia, Y. Li, S. Zhan, Efficient photocatalytic oxygen activation by oxygen-vacancy-rich CeO2-based heterojunctions: Synergistic effect of photoexcited electrons transfer and oxygen chemisorption, Appl. Catal. B: Environ. 289 (2021), 120020, https://doi.org/10.1016/j.apcatb.2021.120020.

[6] X. Ye, Y. Li, P. Luo, B. He, X. Cao, T. Lu, Iron sites on defective BiOBr nanosheets: Tailoring the molecular oxygen activation for enhanced photocatalytic organic synthesis, Nano Res. 15 (2022) 1509–1516, https://doi.org/10.1007/s12274-021-3695-2.

[7] D. Xu, G. Li, Y. Dong, Q. Wang, J. Zhang, T. Yang, S. Pang, G. Zhang, L. Lv, Y. Xia, Z. Ren, P. Wang, Photocatalytic O2 activation enhancement and algae inactivation mechanism of BiO2−x/Bi3NbO7 van der Waals heterojunction, Appl. Catal. B: Environ. 312 (2022), 121402, https://doi.org/10.1016/j.apcatb.2022.121402.

[8] R. Kuriki, K. Sekizawa, O. Ishitani, K. Maeda, Visible-light-driven CO2 reduction with carbon nitride: enhancing the activity of ruthenium, Catal., Angew. Chem. Int. Ed. 54 (2015) 2406–2409, https://doi.org/10.1002/anie.201411170.

[9] X. Lang, X. Chen, J. Zhao, Heterogeneous visible light photocatalysis for selective organic transformations, Chem. Soc. Rev. 43 (2014) 473–486, https://doi.org/10.1039/C3CS60188A.

[10] M.S. Nasir, G. Yang, I. Ayub, S. Wang, L. Wang, X. Wang, W. Yan, S. Peng, S. Ramakarishna, Recent development in graphitic carbon nitride based photocatalysis for hydrogen generation, Appl. Catal. B: Environ. 257 (2019), 117855, https://doi.org/10.1016/j.apcatb.2019.117855.

[11] M. Bellardita, E.I. Garcia-Lopez, G. Marci, I. Krivtsov, J.R. Garcia, L. Palmisano, Selective photocatalytic oxidation of aromatic alcohols in water by using P-doped g-C3N4, Appl. Catal. B: Environ. 220 (2018) 222–233, https://doi.org/10.1016/j.apcatb.2017.08.033.

[12] L. Shi, T. Wang, H. Zhang, K. Chang, J. Ye, Electrostatic self-assembly of nanosized carbon nitride nanosheet onto a zirconium metal-organic framework for enhanced photocatalytic CO2 reduction, Adv. Funct. Mater. 25 (2015) 5360–5367, https://doi.org/10.1002/adfm.201502253.

[13] D. Huang, Z. Li, G. Zeng, C. Zhou, W. Xue, X. Gong, X. Yan, S. Chen, W. Wang, M. Cheng, Megamerger in photocatalytic field: 2D g-C3N4 nanosheets serve as support of 0D nanomaterials for improving photocatalytic performance, Appl. Catal. B: Environ. 240 (2019) 153–173, https://doi.org/10.1016/j.apcatb.2018.08.071.

[14] Q. Liu, J. Shen, X. Yu, X. Yang, W. Liu, J. Yang, H. Tang, H. Xu, H. Li, Y. Li, J. Xu, Unveiling the origin of boosted photocatalytic hydrogen evolution in simultaneously (S, P, O)-Co-doped and exfoliated ultrathin g-C3N4 nanosheets, Appl. Catal. B: Environ. 248 (2019) 84–94, https://doi.org/10.1016/j.apcatb.2019.02.020.

[15] J. Zhang, M. Zhang, R.-Q. Sun, X. Wang, A facile band alignment of polymeric carbon nitride semiconductors to construct isotype heterojunctions, Angew. Chem. Int. Ed. 51 (2012) 10145–10149, https://doi.org/10.1002/anie.201205333.

[16] P. Yang, H. Zhuzhang, R. Wang, W. Lin, X. Wang, Carbon vacancies in a melon polymeric matrix promote photocatalytic carbon dioxide conversion, Angew. Chem. Int. Ed. 58 (2019) 1134–1137, https://doi.org/10.1002/anie.201810648.

[17] Z. Zhu, Y. Ni, Q. Lv, J. Geng, W. Xiea, F. Li, J. Chen, Surface plasmon mediates the visible light-responsive lithium-oxygen battery with Au nanoparticles on defective carbon nitride, Proc. Natl. Acad. Sci. U. S. A. 118 (2021), e2024619118, https://doi.org/10.1073/pnas.2024619118.

[18] T. Gan, J. Yang, D. Morris, X. Chu, P. Zhang, W. Zhang, Y. Zou, W. Yan, S.-H. Wei, G. Liu, Electron donation of non-oxide supports boosts O2 activation on nano-platinum catalysts, Nat. Commun. 12 (2021) 2741, https://doi.org/10.1038/s41467-021-22946-y.

[19] Z. Zhu, Q. Lv, Y. Ni, S. Gao, J. Geng, J. Liang, F. Li, Internal electric field and interfacial bonding engineered step-scheme junction for a visible-light-involved lithium-oxygen battery, Angew. Chem. Int. Ed. 61 (2022), e202116699, https://doi.org/10.1002/anie.202116699.

[20] H. Ben, Y. Liu, X. Liu, X. Liu, C. Ling, C. Liang, L. Zhang, Diffusion-controlled Z-scheme-steered charge separation across PDI/BiOI heterointerface for ultraviolet, visible, and infrared light-driven photocatalysis, Adv. Funct. Mater. 31 (2021) 2102315, https://doi.org/10.1002/adfm.202102315.

[21] X. Wang, X. Wang, J. Huang, S. Li, A. Meng, Z. Li, Interfacial chemical bond and internal electric field modulated Z-scheme S-v-ZnIn2S4/MoSe2 photocatalyst for efficient hydrogen evolution, Nat. Commun. 12 (2021) 4112, https://doi.org/10.1038/s41467-021-24511-z.

[22] L. Chen, X. Yang, J. Chen, J. Liu, H. Wu, H. Zhan, C. Liang, M. Wu, Continuous shape- and spectroscopy-tuning of hematite nanocrystals, Inorg. Chem. 49 (2010) 8411–8420, https://pubs.acs.org/doi/10.1021/ic100919a.

[23] G. Kresse, J. Hafner, Ab initio molecular dynamics for liquid metals, Phys. Rev. B. 47 (1993) 558–561, https://doi.org/10.1103/PhysRevB.47.558.

[24] G. Kresse, J. Furthmiiller, Efficiency of ab-initio total energy calculations for metals and semiconductors using a plane-wave basis set, Comput. Mater. Sci. 6 (1996) 15–50, https://doi.org/10.1016/0927-0256(96)00008-0.

[25] H. Liu, K. Tian, J. Ning, Y. Zhong, Z. Zhang, Y. Hu, One-step solvothermal formation of pt nanoparticles decorated Pt2+-Doped alpha-Fe2O3 nanoplates with enhanced photocatalytic O2 evolution, ACS Catal. 9 (2019) 1211–1219, https://doi.org/10.1021/acscatal.8b03819.

[26] A. Thomas, A. Fischer, F. Goettmann, M. Antonietti, J.-O. Mueller, R. Schloegl, J. M. Carlsson, Graphitic carbon nitride materials: variation of structure and morphology and their use as metal-free catalysts, J. Mater. Chem. A. 18 (2008) 4893–4908, https://doi.org/10.1039/B800274F.

[27] X. Zhang, P. Ma, C. Wang, L. Gan, X. Chen, P. Zhang, Y. Wang, H. Li, L. Wang, X. Zhou, K. Zheng, Unraveling the dual defect sites in graphite carbon nitride for

ultra-high photocatalytic H_2O_2 evolution, Energ. Environ. Sci. 15 (2022) 830–842, https://doi.org/10.1039/D1EE02369A.

[28] C. Lv, Y. Qian, C. Yan, Y. Ding, Y. Liu, G. Chen, G. Yu, Defect engineering metal-free polymeric carbon nitride electrocatalyst for effective nitrogen fixation under ambient conditions, Angew. Chem. Int. Ed. 57 (2018) 10246–10250, https://doi.org/10.1002/anie.201806386.

[29] P. Yang, H. Ou, Y. Fang, X. Wang, A facile steam reforming strategy to delaminate layered carbon nitride semiconductors for photoredox catalysis, Angew. Chem. Int. Ed. 56 (2017) 3992–3996, https://doi.org/10.1002/anie.201700286.

[30] J.A. Singh, S.H. Overbury, N.J. Dudney, M. Li, G.M. Veith, Gold nanoparticles supported on carbon nitride: influence of surface hydroxyls on low temperature carbon monoxide oxidation, ACS Catal. 2 (2012) 1138–1146, https://doi.org/10.1021/cs3001094.

[31] Q. Yi, J. Ji, B. Shen, C. Dong, J. Liu, J. Zhang, M. Xing, Singlet oxygen triggered by superoxide radicals in a molybdenum cocatalytic fenton reaction with enhanced REDOX activity in the environment, Environ. Sci. Technol. 53 (2019) 9725–9733, https://doi.org/10.1021/cs3001094.

[32] L. Wang, X. Zheng, L. Chen, Y. Xiong, H. Xu, Van der Waals heterostructures comprised of ultrathin polymer nanosheets for efficient Z-scheme overall water splitting, Angew. Chem. Int. Ed. 57 (2018) 3454–3458, https://doi.org/10.1002/anie.201710557.

[33] P. Wang, Z. Shen, Y. Xia, H. Wang, L. Zheng, W. Xi, S. Zhan, Atomic insights for optimum and excess doping in photocatalysis: a case study of few-layer Cu-ZnIn$_2$S$_4$, Adv. Funct. Mater. 29 (2019) 1807013, https://doi.org/10.1002/adfm.201807013.

[34] Z. Zhou, Z. Shen, C. Song, M. Li, H. Li, S. Zhan, Boosting the activation of molecular oxygen and the degradation of tetracycline over high loading Ag single atomic catalyst, Water Res. 201 (2021), 117314, https://doi.org/10.1016/j.watres.2021.117314.

[35] D. Zhao, C.-L. Dong, W. Bin, C. Chen, Y.-C. Huang, Z. Diao, S. Li, L. Guo, S. Shen, Synergy of dopants and defects in graphitic carbon nitride with exceptionally modulated band structures for efficient photocatalytic oxygen evolution, Adv. Mater. 31 (2019) 1903545, https://doi.org/10.1002/adma.201903545.

[36] J. Wang, Y. Yu, J. Cui, X. Li, Y. Zhang, C. Wang, X. Yu, J. Ye, Defective g-C$_3$N$_4$/covalent organic framework van der Waals heterojunction toward highly efficient S-scheme CO$_2$ photoreduction, Appl. Catal. B: Environ. 301 (2022), 120814, https://doi.org/10.1016/j.apcatb.2021.120814.

[37] Y. Nosaka, A.Y. Nosaka, Generation and detection of reactive oxygen species in photocatalysis, Chem. Rev. 117 (2017) 11302–11336, https://doi.org/10.1021/acs.chemrev.7b00161.

[38] J. Wang, D. Zhi, H. Zhou, X. He, D. Zhang, Evaluating tetracycline degradation pathway and intermediate toxicity during the electrochemical oxidation over a Ti/Ti$_4$O$_7$ anode, Water Res. 137 (2018) 324–334, https://doi.org/10.1016/j.watres.2018.03.030.